


Piezoresistance in ballistic graphene

Abhinaba Sinha^{✉,*}, Abhishek Sharma,[†] Ashwin Tulapurkar, V Ramgopal Rao, and Bhaskaran Muralidharan^{✉,‡}
 Department of Electrical Engineering, IIT Bombay, Powai, Mumbai-400076, India

 (Received 28 June 2019; revised manuscript received 9 November 2019; published 30 December 2019)

We investigate the longitudinal and transverse piezoresistance effect in suspended graphene in the ballistic regime. Utilizing parametrized tight-binding Hamiltonian along with Landauer quantum transport formalism, we devise a methodology to evaluate the piezoresistance effect in graphene. We evaluate the longitudinal and transverse gauge factor of graphene along armchair and zigzag directions in the linear elastic limit (0%–10%). The gauge factors along armchair and zigzag directions are identical. Our model predicts a significant enhancement ($\approx 1000\%$) in the value of transverse gauge factor compared to longitudinal gauge factor along with sign inversion. The calculated value of longitudinal gauge factor is ≈ 0.3 , whereas the transverse gauge factor is ≈ -3.3 . We rationalize our prediction based on the deformation of Dirac cone and change in separation between transverse modes due to longitudinal and transverse strain. The results obtained herein can serve as a template for high-strain piezoresistance effect of graphene in nanoelectromechanical systems.

DOI: [10.1103/PhysRevMaterials.3.124005](https://doi.org/10.1103/PhysRevMaterials.3.124005)

I. INTRODUCTION

Graphene became one of the most extensively researched materials soon after its discovery in 2004. It is the first single-atom-thick two-dimensional (2D) material isolated in the laboratory. Owing to its unique properties, it is often termed as a “wonder material” [1] or a “miracle material” [2]. Graphene is one of the strongest known materials [3] and thus undergoes elastic deformation for more than 20% strain [4,5]. Due to these exceptional mechanical properties, graphene is an excellent material for strain engineering.

Early attempts of graphene-strain-engineering began in 2008 with the prediction of the presence of a pseudomagnetic field due to a nonuniform strain distribution, leading to a zero field quantum Hall effect [6–8]. Subsequent *ab initio* studies of the band structure showed Dirac cone shift, anisotropic fermi velocity, and band gap opening beyond 20% uniaxial strain [9–12]. Later, these predictions were experimentally verified using Raman spectroscopy [13] and anisotropic resistance measurements with strain [5]. Moreover, graphene shows superconductivity at a certain doping concentration along with the application of a biaxial strain [14]. Also, band gap is formed in graphene by self assembly of H atoms along with the application of a compressive strain [15]. All these distinct features helped in the evolution of graphene as a suitable material for flexible electronics [16–18].

Another important application of strain engineering is the piezoresistance effect. Piezoresistance is mainly used in strain sensing [19]. Piezoresistance effect in graphene membrane has been investigated previously in diffusive regime and near ballistic regime of transport. The value of gauge factor reported for suspended graphene lies between 1.25 and 6.73

[19–21]. Piezoresistance in graphene strongly depends on the type of graphene [20,22], the substrate underneath [23–25], and the scattering mechanism involved [19].

Despite the rapid miniaturization of the size of electromechanical systems and the dimension of graphene in these systems typically reducing below its mean free path, piezoresistance effect in ballistic graphene is still unexplored. Since, the electron transport mechanism in a ballistic conductor is entirely different from that of a diffusive conductor, piezoresistance in ballistic graphene may eventually show new outcomes, leading to novel straintronics applications.

Graphene sheet exhibits 2D characteristics for width beyond 100 nm [26] and has a very high value of mean free path in the submicron range [27–29]. Thus, graphene behaves as a 2D ballistic conductor for width more than 100 nm and less than its mean free path.

In this paper, we explore the piezoresistance effect in ballistic graphene along armchair and zigzag directions. We develop a generic theoretical model for gauge factor (GF) of graphene in ballistic regime. This model computes GF from mode density using band counting method [30] and Landauer formalism.

In the subsequent sections, we describe the mathematical model, calculate the transport properties and GF of graphene, and explain the underlying physics of the predicted value of longitudinal gauge factor (LGF) and transverse gauge factor (TGF) along armchair and zigzag directions. The derivation of mathematical expressions are elaborated in the Appendices.

II. THEORETICAL MODEL

A. Simulation setup

The setups S_1 and S_2 consist of a graphene sheet having contacts C_1 and C_2 across the zigzag direction (y axis) and armchair direction (x axis) as shown in Figs. 1(a) and 1(b), respectively. A uniaxial strain (ϵ_y) in the linear elastic regime (0%–10%) [31] is applied along zigzag direction in S_1 and

*asinha@iitb.ac.in

†sabhishek.iitb@gmail.com

‡Corresponding author: bm@ee.iitb.ac.in

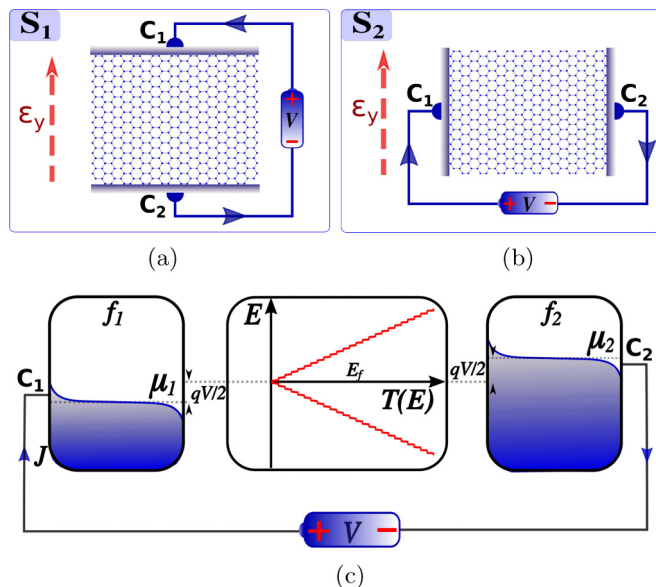


FIG. 1. Schematic diagram of simulation setups S_1 and S_2 to determine the LGF and TGF of graphene. A uniaxial strain ε_y is applied along the zigzag direction (y axis) in both setups. (a) Setup S_1 consists of a voltage source (V) connected across the zigzag direction, using contacts C_1 and C_2 . Similarly, (b) setup S_2 consists of a voltage source (V) connected across the armchair direction, using contacts C_1 and C_2 . (c) A generic quantum transport model for S_1 and S_2 is shown with contacts C_1 and C_2 connected across the graphene sheet having transmission $T(E)$.

S_2 . The magnitude of strain is gradually increased from 0% to 10% and simultaneously, the current density (J) is obtained for an applied voltage (V) in the linear regime ($|V| \leq 0.01$ eV). The LGF is obtained from setup S_1 , whereas the TGF is obtained from setup S_2 for zigzag direction. The LGF and TGF for armchair direction are also evaluated in a similar manner.

The quantum transport model for S_1 and S_2 is shown in Fig. 1(c). The Fermi energy of the graphene channel (E_f) is at 0 eV. The Fermi function at C_1 is f_1 with fermi energy at $\mu_1 = -qV/2$. Similarly, the Fermi function at C_2 is f_2 with Fermi energy at $\mu_2 = qV/2$. For ease of calculation, armchair direction is taken along the x axis and zigzag direction is taken along the y axis.

We sketch in Fig. 2, a generic computational model that evaluates GF of a 2D material in the ballistic regime. We employ this model to compute LGF and TGF of graphene along zigzag and armchair directions. Our model involves obtaining the Brillouin zone, calculating the band structure of strained graphene using parametrized tight-binding Hamiltonian, evaluation of the mode density function of graphene using the band counting method [30] and finally evaluation of GF using Landauer formalism. The detailed description of these steps are as follows:

1. Brillouin zone and E - k relation of strained graphene

Basis vectors \vec{a}_1^i and \vec{a}_2^i describe the crystal-lattice of uniaxially strained graphene along armchair and zigzag

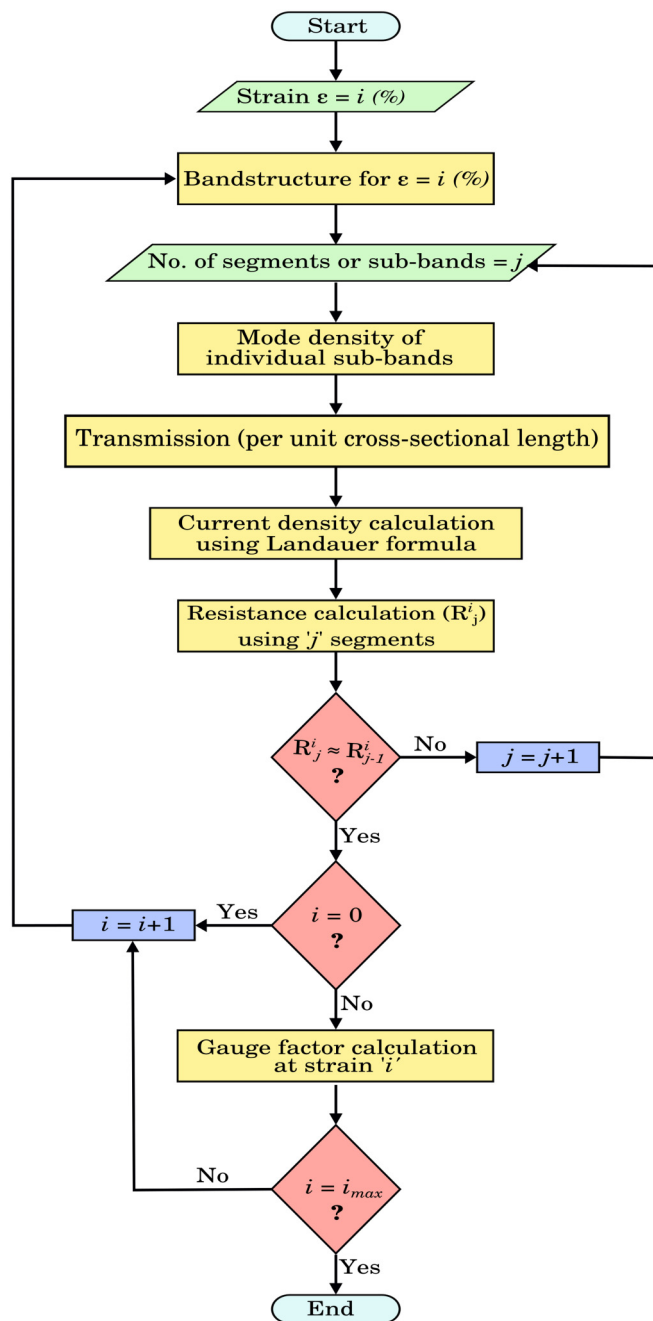


FIG. 2. Flow chart for gauge factor (GF) calculation of a 2D material in the ballistic regime. “ i ” is the percentage strain, “ j ” is the number of segments or sub-bands used in the band counting method, “ R_j^i ” is the resistance with “ j ” segments and i_{\max} is the maximum linear elastic limit of the 2D material.

directions. Superscript “ i ” denotes the magnitude of strain ε_x along x axis and ε_y along y axis in percentage. Figure 3(a) shows schematic diagram of \vec{a}_1^i and \vec{a}_2^i in uniaxially strained graphene crystal. The basis vectors \vec{a}_1^i and \vec{a}_2^i are given by

$$\vec{a}_1^i = a^i \hat{x} + b^i \hat{y}, \quad (1)$$

$$\vec{a}_2^i = a^i \hat{x} - b^i \hat{y}, \quad (2)$$

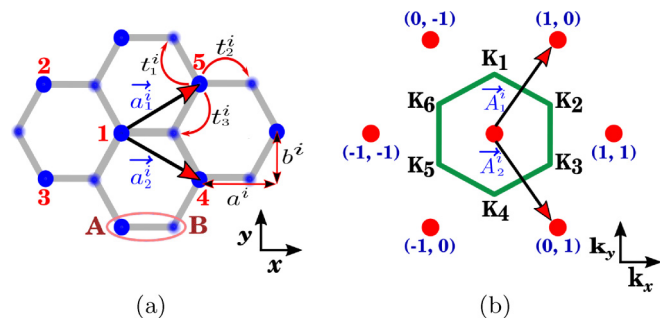


FIG. 3. (a) Real crystal lattice of strained graphene with \vec{a}_1^i, \vec{a}_2^i as basis vectors, A-B as basis, and $t_1^i, t_2^i,$ and t_3^i as nearest-neighbor tight-binding parameters. (b) Reciprocal crystal lattice and first Brillouin zone of strained graphene with reciprocal basis vectors \vec{A}_1^i and \vec{A}_2^i . The intersection of the edges of Brillouin zone are labeled as K_1, K_2, \dots, K_6 in clockwise manner and their corresponding Dirac points are denoted by DP_1, DP_2, \dots, DP_6 , respectively.

where $a^i = 1.5a_0(1 + \epsilon_x)$ and $b^i = (\sqrt{3}/2)a_0(1 + \nu\epsilon_x)$ for armchair strained graphene. Similarly $a^i = 1.5a_0(1 + \nu\epsilon_y)$ and $b^i = (\sqrt{3}/2)a_0(1 + \epsilon_y)$ for zigzag strained graphene. Figure 3(b) shows the corresponding Brillouin zone of strained graphene. The reciprocal basis vectors corresponding to Eqs. (1) and (2) are given by

$$\vec{A}_1^i = \frac{\pi}{a^i}\hat{k}_x + \frac{\pi}{b^i}\hat{k}_y, \quad (3)$$

$$\vec{A}_2^i = \frac{\pi}{a^i}\hat{k}_x - \frac{\pi}{b^i}\hat{k}_y. \quad (4)$$

Graphene behaves elastically up to 20% strain [3–5]. Here, we apply strain in the range of 0%–10% that corresponds to the linear elastic regime in graphene [31]. The magnitude of Poisson's ratio ($\nu = \frac{\epsilon_t}{\epsilon_l}$) for uniaxial strain in graphene has been reported in the range of 0.10–0.186 [4,9,11]. We use $\nu = -0.14$ and $a_0 = 1.42 \text{ \AA}$ in all our calculations [29]. The corresponding reciprocal lattice points are given by

$$\vec{G}^i = M\vec{A}_1^i + N\vec{A}_2^i. \quad (5)$$

The reciprocal lattice points nearest to the origin are shown with red dots in Fig. 3(b). A generic first Brillouin zone for uniaxially strained graphene along armchair direction or zigzag direction is shown in Fig. 3(b) as a green hexagon.

The nearest-neighbor parametrized tight-binding expression for band structure of strained graphene is given by

$$E^i(k) = \pm |t_1^i e^{-ik \cdot \vec{a}_1^i} + t_2^i + t_3^i e^{-ik \cdot \vec{a}_2^i}|. \quad (6)$$

We obtain the hopping parameters $t_1^i, t_2^i,$ and t_3^i for strained graphene from Ribeiro *et al.* (see Appendix A) [11]. They extracted the tight-binding parameters by fitting the band structure obtained from *ab initio* calculations with Eq. (6). The analytical tight-binding model described by Eq. (6) for strained graphene was studied by Pereira *et al.* [31]. This model does not consider the overlap factors of the orbitals. Thus, Eq. (6) is insufficient to fit the entire band structure in first Brillouin zone. It can generate band structure accurately for energy less than 0.2 eV, i.e., within Dirac cone approximation. Furthermore, Eq. (6) accurately describes Dirac

cone shift and anisotropy in Fermi velocity due to strain [5,12,13,31]. Thus, Eq. (6) is an accurate representation of the band structure of strained graphene for energy less than 0.2 eV. In this work, we use Landauer formalism [Eq. (10)] which is also valid in this energy range. Therefore, the mode density is very precisely determined by Eq. (6). Using band structures at different strain in the first Brillouin zone, we compute mode density at different strain.

2. Mode density calculation

The most essential step in GF calculation is determination of the mode density. The two prominent methods used to obtain mode density function in ballistic conductors are as follows:

(1) Band counting method.

(2) Non-equilibrium green's function method (NEGF).

Among these two methods, band counting method is a relatively simpler technique for mode density calculation, provided dispersion relation is known. Transverse modes (TMs) are quantum confined energy states in the transverse direction to the electron transport. Each point in the energy dispersion of a TM acts as a channel for electron transport at that energy and is known as a mode. By counting the number of TMs crossing a particular energy, modes at that particular energy is obtained. The total modes as a function of energy is known as the mode density function or mode density. The method discussed above is known as band counting method. It was successfully used to compute the thermoelectric properties of germanium by Jeong *et al.* [30].

For a 2D material like graphene whose conduction band and valence band meet at a single point, mode density calculation near the Dirac point is a challenging task. Thus, we compute the mode density function of graphene using a numerical technique that implements the band counting method in 2D materials. Once the mode density is calculated for graphene, GF can be easily obtained.

Figure 2 illustrates the flowchart for implementation of band counting method in 2D materials. The numerical method is described as follows:

The first Brillouin zone of graphene is divided into “ j ” segments of equal width along the transverse direction. Each segment encloses a portion of the Brillouin zone between two successive dotted lines as shown in Figs. 4(a) and 4(b). The width of the segments at the edges are half of that of the intermediate segments. Each segment contains several TMs. The TM passing through the center of each segment is denoted as k_\perp . For the sake of convenience, we refer to k_\perp as sub-band in this manuscript. k_\perp is shown with a blue line and varies from 1 to 9 in Figs. 4(a) and 4(b). The width of an intermediate segment is Δk_x in S_1 and Δk_y in S_2 . We assume that all TMs within a segment have same mode density since they are very close to each other in k -space. To effectively calculate the mode density at energies close to the Dirac cone, a large number of segments “ j ” are required. The number of segments “ j ” is varied from 10^2 to 10^4 and simultaneously the resistance is obtained for a $1\text{-}\mu\text{m}$ -wide graphene sheet. The plot of resistance versus the number of segments for S_1 is shown in Fig. 4(c) and S_2 is shown in Fig. 4(d). We observe that the value of resistance does not vary beyond

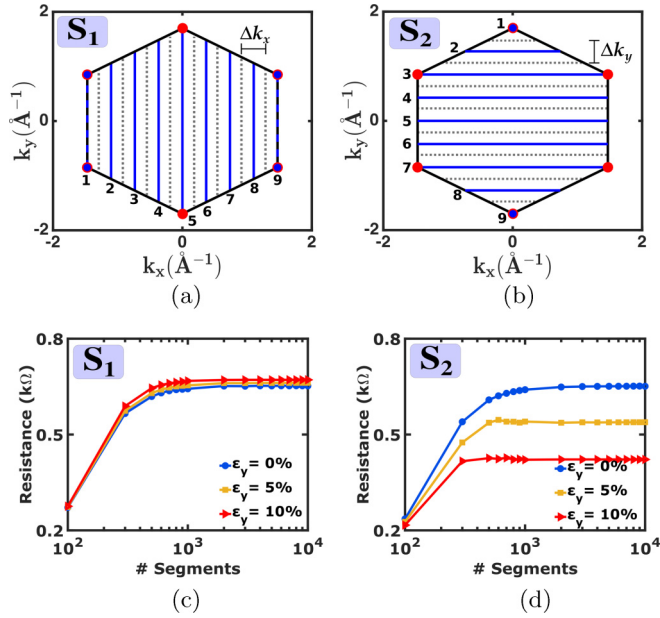


FIG. 4. Sub-bands in the first Brillouin zone of graphene in (a) setup S_1 and (b) setup S_2 for mode density calculation. Nine segments are shown here for representational purpose only. The variation of resistance with number of segments in (c) setup S_1 , and in (d) setup S_2 for 0%, 5%, and 10% strain. The value of resistance becomes constant beyond 1000 segments in S_1 and S_2 .

1000 segments. The transport properties of graphene, namely, transmission, current density, and resistance obtained for more than 1000 segments are the actual values of the transport properties of ballistic graphene. Mode density of the sub-band (k_{\perp}) assuming the presence of “ p ” energy minima and “ q ” energy maxima is given by

$$M_{k_{\perp}}^i(E) = \sum_{p=1}^p \Theta(E \mp E_p^i) - \sum_{q=1}^q \Theta(E \mp E_q^i). \quad (7)$$

The negative sign in Eq. (7) is for conduction band, whereas the positive sign is for valence band. The detail derivation of Eq. (7) is given in Appendix B.

Figures 4(a) and 4(b) show the Brillouin zone with nine segments for transport along zigzag direction and armchair direction respectively. The collective mode density (per unit cross-sectional length) of all TMs in the region Δk_x or Δk_y , containing the sub-band “ k_{\perp} ” is given by

$$T_{k_{\perp}}^i(E) = P_{k_{\perp}}^i * M_{k_{\perp}}^i(E), \quad (8)$$

where $P_{k_{\perp}}^i$ is the prefactor and $M_{k_{\perp}}^i$ is the mode density of the sub-band “ k_{\perp} .” For the edge sub-bands (with $k_{\perp} = 1$ and j) in Figs. 4(a) and 4(b), the prefactors are P_1^i and P_j^i , and for the intermediate segments (with $k_{\perp} = 2$ to $j-1$), the prefactor is $P_{k_{\perp}}^i$, where $P_1^i = P_j^i = P_{k_{\perp}}^i/2$ and $P_{k_{\perp}}^i = \Delta k/(2\pi)$ (see Appendix B). The total mode density or transmission per unit cross-sectional length of ballistic graphene is given by

$$T^i(E) = P_1^i M_1^i(E) + \sum_{k_{\perp}=2}^{j-1} P_{k_{\perp}}^i M_{k_{\perp}}^i(E) + P_j^i M_j^i(E). \quad (9)$$

For detail derivation of Eq. (9), see Appendix B.

3. Evaluation of gauge factor (GF) in ballistic regime

Landauer equation for current density [$J^i(V)$] [32] is given by

$$J^i(V) = \frac{2q}{h} \int_{-\infty}^{\infty} T^i(E) [f_1(E - \mu_1) - f_2(E - \mu_2)] dE. \quad (10)$$

Equation (10) is valid in linear regime, i.e., a few kT 's near the Fermi energy, where kT is thermal energy at room temperature. The voltage varies from -0.01 V to 0.01 V, whereas the energy limit in Eq. (10) varies from -0.2 eV to 0.2 eV. r^i is the gradient of voltage and current density. It is defined as

$$r^i = \frac{dV}{dJ^i}. \quad (11)$$

The expression for resistance (R^i) is given by

$$R^i = \frac{r^i}{L_{cs}(1 + \nu\varepsilon)}, \quad (12)$$

where, L_{cs} is the cross sectional length of graphene at 0% strain, ν is the Poisson's ratio, and ε is ε_x or ε_y , depending on the direction of strain. Finally, the expression for GF is given by

$$GF = \frac{R^i - R^0}{R^0\varepsilon} = \frac{1}{\varepsilon} \left[\frac{r^i}{r^0(1 + \nu\varepsilon)} - 1 \right], \quad (13)$$

where R^0 is the value of resistance at 0% strain and R^i is the resistance at i % strain.

4. Evaluation of gauge factor (GF) in diffusive regime

The length of a diffusive conductor is much larger than its mean free path. In diffusive regime of transport, Boltzman transport theory is commonly used. Using linearized Boltzman transport theory, Peres *et al.* [33] have phenomenologically obtained an expression for conductivity of graphene considering screened Coulombic impurities as the prime source of scattering.

The conductivity predicted using Coulombic impurities in graphene is linearly dependent on the electron density. This result is in accordance with the experimentally observed conductivity [28,34]. The expression for conductivity obtained by Peres *et al.* is given by

$$\sigma = \frac{2e^2\pi(\hbar v_f)^2 n}{hu_o^2}, \quad (14)$$

where u_o is the scattering potential, v_f is the fermi velocity and n is the electron density.

The expressions for LGF and TGF obtained from Eq. (14) are given by

$$LGF = 1 + |\nu| - 2 \frac{\Delta v_f/v_f}{\varepsilon}, \quad (15)$$

$$TGF = -(1 + |\nu|) - 2 \frac{\Delta v_f/v_f}{\varepsilon}. \quad (16)$$

For detail derivation of Eqs. (15) and (16), see Appendix D.

III. RESULTS AND DISCUSSIONS

In this section, we discuss the strain-dependent transport properties along zigzag direction in the ballistic regime. We

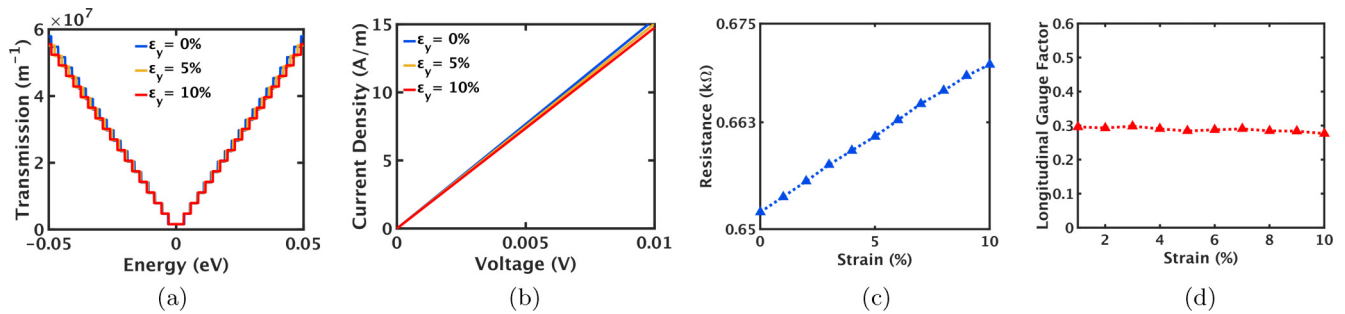


FIG. 5. Strain (ϵ_y)-dependent transport properties in setup S_1 of graphene. (a) Plot of transmission versus energy for 0%, 5% and 10% strain. Transmission decreases with an increase in strain. (b) Plot of current density versus voltage at 0%, 5%, and 10% strain. The magnitude of current density decreases with strain. (c) Plot of resistance versus strain of a 1- μ m-wide graphene sheet. The resistance increases linearly with strain. (d) Plot of longitudinal gauge factor versus strain. The average LGF is ≈ 0.3 .

further evaluate the longitudinal and transverse gauge factor along the zigzag direction and then compare it with that of the armchair direction. We compare the GFs in ballistic regime with that of the diffusive regime and other previously reported works. The piezoresistance effect in ballistic graphene is due to the distortion of Dirac cones and change in separation of TMs with applied strain, whereas in diffusive regime, it is due to the change in Fermi velocity [33]. The transport properties of S_1 and S_2 are shown in Figs. 5 and 6, respectively.

We have calculated the value of resistivity equal to 1.3 k Ω at 0% strain which is within the resistivity range (1.2–1.6 k Ω) calculated previously for suspended graphene [27].

The transmission increases with energy at a particular strain, as shown in Figs. 5(a) and 6(a). It can be inferred from Fig. 5(a) that in setup S_1 with an applied strain, the transmission decreases due to a decrease in the mode density as explained in the subsequent subsections. This reduction in transmission with increase in strain leads to a reduction in current density [Fig. 5(b)] and finally an increase in the resistance [Fig. 5(c)]. The average LGF is 0.3 [Fig. 5(d)]. Whereas, in setup S_2 , the transmission increases significantly with applied strain as shown in Fig. 6(a). As a result, the current density increases substantially in Fig. 6(b) and finally the resistance decreases in Fig. 6(c). The average TGF is -3.3 [Fig. 6(d)].

Here, we demonstrate a larger value of TGF (≈ 10 times) compared to LGF. Moreover, the piezoresistance characteris-

tics of armchair configuration is same as that of the zigzag configuration (see Fig. 7). Using Eqs. (15) and (16), we obtain LGF and TGF equal to 1.3 and -1.14 , respectively, for diffusive regime. The LGF in diffusive regime depends on Fermi velocity, whereas the TGF is independent of Fermi velocity provided electron density remain constant. Previous studies on GF of graphene in diffusive regime have measured LGF around 1.9–2.92 [19,20], which is close to the value predicted in this work. We see that the magnitude of LGF and TGF are nearly same in diffusive regime with an inverse sign. The LGF and TGF of ballistic graphene have large difference in magnitude ($\approx 1000\%$) with an inverse sign. The physics behind the sizable variation of LGF and TGF are elaborately explained later.

The linearly varying resistance in S_1 [Fig. 5(c)] and S_2 [Fig. 6(c)] with strain are very useful in strain sensing. These results suggest that suspended graphene can be used as high-strain sensors by suitable calibration. Setup S_2 is more sensitive to strain than setup S_1 due to the higher value of GF. High-strain sensors are very useful in flexible electronics [5]. They have been studied previously for zinc oxide nanowire based flexible films [35] and graphene-rubber composite [36].

A. Effect of strain on Dirac cone

The linear regime energy in graphene corresponds to energy close to the Dirac points. Therefore, we analyze the

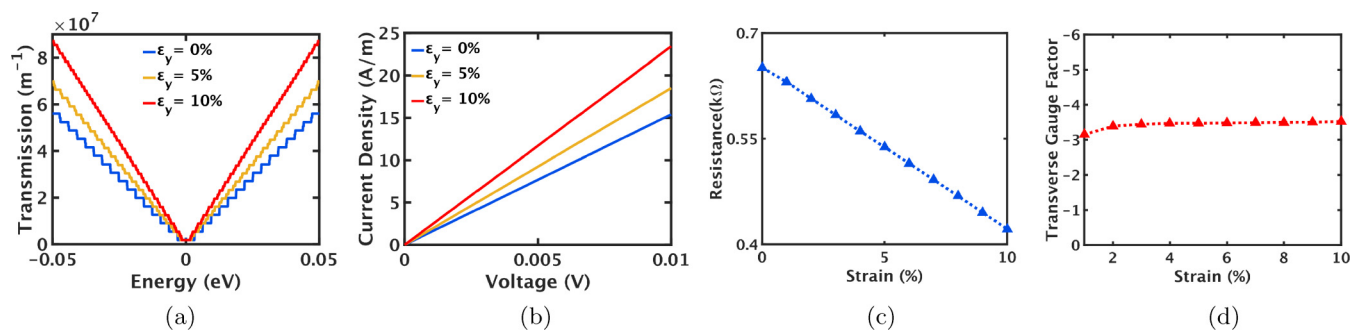


FIG. 6. Strain (ϵ_y)-dependent transport properties in setup S_2 of graphene. (a) Plot of transmission versus energy for 0%, 5%, and 10% strain. The transmission increases with an increase in strain. (b) Plot of current density versus voltage at 0%, 5%, and 10% strain. The magnitude of current density increases with strain. (c) Plot of transverse resistance versus strain of a 1- μ m-wide graphene sheet. The resistance decreases linearly with strain. (d) Plot of transverse gauge factor versus strain. The average TGF is ≈ -3.3 .

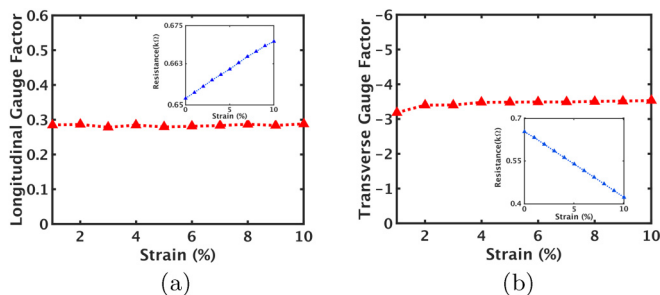


FIG. 7. (a) The longitudinal gauge factor (LGF) of graphene for strain along the armchair direction. (b) The transverse gauge factor (TGF) of graphene for strain along the armchair direction. The plot of resistance versus strain of a $1\text{-}\mu\text{m}$ -wide graphene sheet is shown as inset figures in (a) and (b). The gauge factors (GF) of armchair graphene are the same as zigzag graphene.

effect of strain on a Dirac cone to understand the cause of piezoresistance in graphene.

Graphene undergoes elastic deformation for more than 20% of strain [4,5]. Simultaneously, it is highly resistive to band gap opening and undergoes band opening beyond 23% of strain along the zigzag direction [9–11]. In contrast, band gap does not open with applied strain along the armchair direction. The Dirac points shift their position from K-points due to the applied strain [10,11,31]. Moreover, strain induces anisotropy in Fermi velocity along the longitudinal and transverse direction as a result of deformation of the Dirac cones [5,13,31]. In this work, we restrict our discussion to 10% uniaxial strain only.

The shift in Dirac points DP_1 and DP_2 with respect to K_1 and K_2 at 10% strain along armchair and zigzag directions are illustrated in Figs. 8(a) and 8(b), respectively. Table I lists the relative shift in reciprocal space between K_1 and DP_1 , and K_2 and DP_2 with strain. For strain along the armchair direction, Dirac points DP_1 and DP_4 move inside the Brillouin zone and Dirac points DP_2 , DP_3 , DP_5 , and DP_6 move away from the Brillouin zone [Fig. 8(a)]. For strain along the zigzag direc-

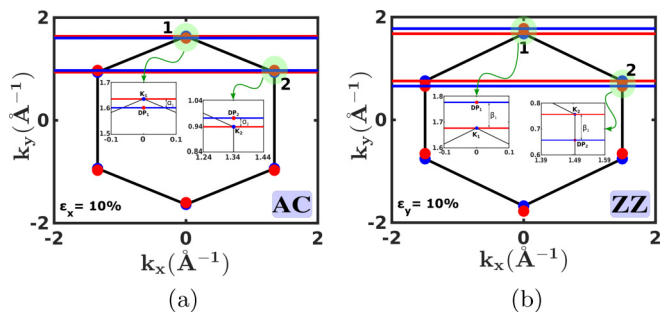


FIG. 8. (a) Shift in Dirac points DP_1 (α_1) and DP_2 (α_2) due to strain ($\epsilon_x = 10\%$) along armchair direction. DP_1 moves inside the Brillouin zone along the line joining K_1 and K_4 whereas DP_2 moves out of the Brillouin zone along the line joining K_2 and K_3 . (b) Shift in Dirac points DP_1 (β_1) and DP_2 (β_2) due to strain ($\epsilon_y = 10\%$) along zigzag direction. DP_1 moves out of the Brillouin zone along the line joining K_1 and K_4 , whereas DP_2 moves inside the Brillouin zone along the line joining K_2 and K_3 . Inset figures in (a) and (b) show the magnified view of the shift in Dirac points DP_1 and DP_2 .

TABLE I. Relative shift in position of Dirac points with respect to K-points with strain (refer to Fig. 8).

Strain $i\%$	S_1 $\alpha_1^i (\text{\AA}^{-1})$	S_1 $\alpha_2^i (\text{\AA}^{-1})$	S_2 $\beta_1^i (\text{\AA}^{-1})$	S_2 $\beta_2^i (\text{\AA}^{-1})$
1%	0.0022	-0.0022	-0.0069	0.0069
5%	0.0137	-0.0137	-0.0401	0.0401
10%	0.0337	-0.0337	-0.0995	0.0994

tion, DP_1 and DP_4 move away from Brillouin zone whereas the Dirac points DP_2 and DP_3 , and DP_5 and DP_6 move closer to each other along the edge of Brillouin zone [see Fig. 8(b)]. We observe an identical response of DP_1 and DP_4 in first Brillouin zone due to strain (see Fig. 8). Similarly, DP_2 , DP_3 , DP_5 , and DP_6 show identical response to strain. The shifting of these two sets of Dirac points with respect to K-points are exactly same but in opposite direction. Therefore, analysis of Dirac cones at DP_1 and DP_2 are sufficient to understand the strain response of other Dirac cones.

In addition to shifting of the Dirac points, strain deforms Dirac cones as well [5,12,13,31]. Application of uniaxial strain deform these Dirac cones into oval shaped cones as

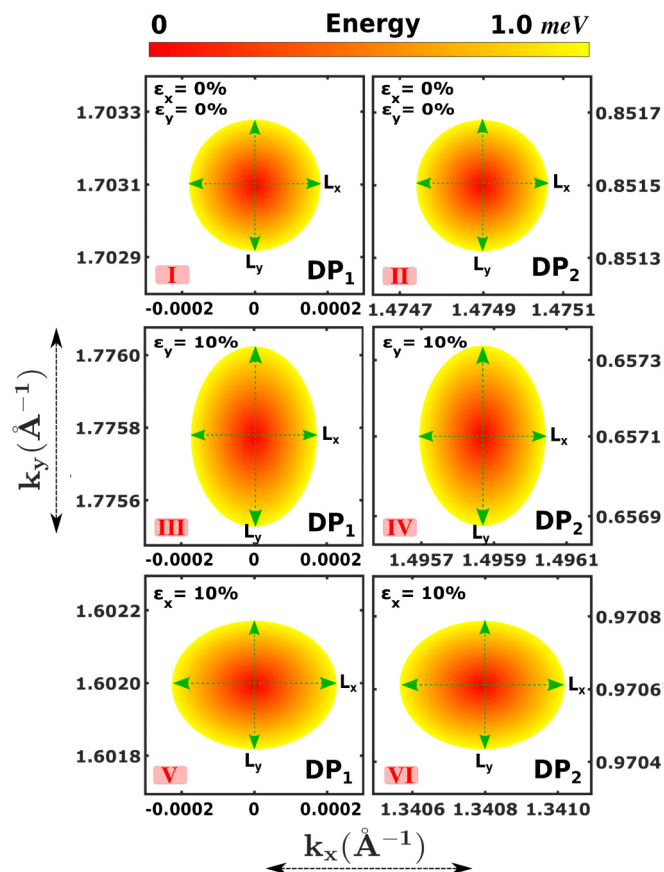


FIG. 9. Top view of the Dirac cones. (I) DP_1 at $\epsilon_x = \epsilon_y = 0\%$. (II) DP_2 at $\epsilon_x = \epsilon_y = 0\%$. (III) DP_1 at $\epsilon_y = 10\%$. (IV) DP_2 at $\epsilon_y = 10\%$. (V) DP_1 at $\epsilon_x = 10\%$. (VI) DP_2 at $\epsilon_x = 10\%$. The dimensions of DP_1 and DP_2 are the same for the same magnitude of strain. The major and minor axes of the Dirac cones are equal for the same magnitude of strain along x and y directions.

TABLE II. Axes length (\AA^{-1}) of Dirac cones with strain at $E = 1$ meV.

Strain $i\%$	$DP_1(S_1)$ (L_x)	$DP_1(S_1)$ (L_y)	$DP_2(S_2)$ (L_x)	$DP_2(S_2)$ (L_y)
0%	0.000361	0.000362	0.000361	0.000362
5%	0.000413	0.000354	0.000354	0.000413
10%	0.000495	0.000347	0.000347	0.000495

illustrated in Fig. 9. From Table II, we see that each Dirac cones have identical deformation for an applied strain. The dimensions of these cones depend only on the magnitude of applied strain. Thus, we conclude that the shape of the Dirac cones do not depend on the tight-binding parameters for strain in linear elastic regime.

In unstrained graphene, each Dirac cone contributes 1/3 to the first Brillouin zone. Effectively, two Dirac cones are present inside the first Brillouin zone. The same is true in the case of uniaxially strained graphene along armchair and zigzag directions (see Fig. 8). In Fig. 8(a), Dirac cones at DP_1 and DP_4 are present inside the first Brillouin zone. Similarly, in Fig. 8(b), a half portion of the Dirac cones at DP_2 , DP_3 , DP_5 , and DP_6 are present inside the first Brillouin zone, the remaining portions lie outside. In other words, effectively only two Dirac cones lie inside the first Brillouin zone of graphene, for strain along armchair direction or zigzag direction.

B. Physics of gauge factor variation

Piezoresistance effect in a ballistic conductor is due to the change in transmission with applied strain. The change in transmission is primarily due to the change in band structure. Owing to the zero band gap in graphene for large value of strain, piezoresistance is due to the deformation of Dirac cones for strain in our range of interest (see Fig. 9).

As discussed earlier, the effective number of Dirac cones in the first Brillouin zone of uniaxially strained graphene is 2 and the Dirac cones are identical in every respect. From Figs. 9 and 10, we conclude that in a Dirac cone the mode density along k_x direction and $-k_x$ direction are same irrespective of the magnitude and direction of strain. As a result, the mode density along armchair direction is numerically equal to the collective mode density along k_x and $-k_x$ directions in a Dirac cone. A similar argument holds for mode density along zigzag direction also. Therefore, we can calculate the mode density of graphene along armchair or zigzag direction from a single Dirac cone. From Table II, we see that the deformation of Dirac cones are the same for the same magnitude of strain along armchair and zigzag directions. Furthermore, the separation between TMs are the same in setup S_1 and S_2 of zigzag and armchair directions because of same width of graphene. Consequently, we obtain the same GF along zigzag and armchair directions.

Figure 10 illustrates TMs at 1 meV constant energy surface of the Dirac cone at 0% and 10% strain in S_1 and S_2 . The parallel dotted lines represent the path of TMs, whereas the red cross marks represent the modes at that particular energy. The number of modes in S_1 reduces from ‘‘M’’ to ‘‘N’’ as the

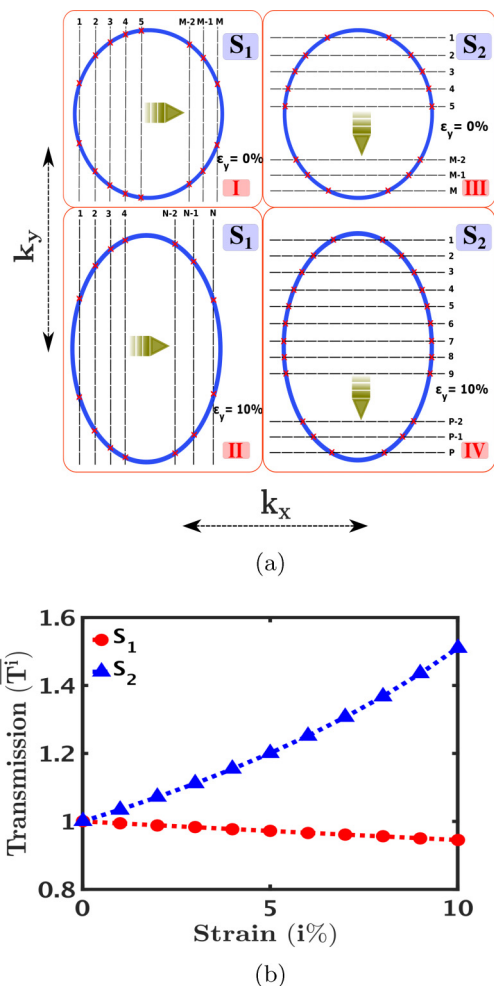


FIG. 10. (a) Schematic diagram of the constant energy surface of a Dirac cone and TMs at 1 meV energy. (I) Dirac cone surface with ‘‘M’’ TMs (red cross) along zigzag direction at 0% strain (S_1). (II) Dirac cone surface with ‘‘N’’ TMs (red cross) along zigzag direction at 10% strain (S_1). (III) Dirac cone surface with ‘‘M’’ TMs (red cross) along armchair direction at 0% strain (S_2). (IV) Dirac cone surface with ‘‘P’’ TMs (red cross) along armchair direction at 10% strain (S_2). (b) The change in normalized transmission as a result of deformation of constant energy surface (1 meV) due to strain in S_1 and S_2 .

strain is increased from 0% to 10% along zigzag directions [see Fig. 10(I) and Fig. 10(II)]. The overall reduction in mode density is due to the small decrease in length of the minor axis of the constant energy surface and small increase in the separation between the TMs due to slight decrease in width as a result of transverse strain (separation between TM = $2\pi/L_{cs}$). Thus, we see a small overall decrease in transmission with strain in S_1 as shown in Fig. 10(b). Whereas in setup S_2 , due to an increase in major axis length of constant energy surface and reduction in separation of TMs, a significant increase in transmission is seen as shown in Fig. 10(b). The change in transmission at any other energy in linear regime is similar to the one discussed above as the major and minor axis of the constant energy surface at different energies are proportional at a definite value of strain. Thus, the total

change in transmission in S_1 and S_2 follows the same trend as shown in Fig. 10(b) for $E = 1$ meV. The ratio of change in transmission at 1 meV energy in S_1 and S_2 is ≈ 10 times which is same as the ratio of the LGF and TGF. This explains the sizable variation in LGF and TGF value obtained in ballistic regime.

IV. CONCLUSION

In this paper, we investigated the longitudinal and transverse piezoresistance in suspended graphene in ballistic regime. Utilizing parametrized tight-binding Hamiltonian along with Landauer quantum transport formalism, we devised a methodology to evaluate the piezoresistance effect in graphene. We computed the longitudinal gauge factor and transverse gauge factor of ballistic graphene along armchair and zigzag directions in the linear elastic limit (0%–10%). The value of gauge factors were same along armchair and zigzag directions. Our model predicted a significant variation ($\approx 1000\%$ increase) in the magnitude of transverse gauge factor compared to longitudinal gauge factor along with sign inversion. The longitudinal gauge factor obtained is ≈ 0.3 whereas the transverse gauge factor is ≈ -3.3 . We rationalized our predictions based on deformation of Dirac cone and change in the separation between transverse modes due to longitudinal and transverse strain. The results obtained in this paper could be useful for future straintronics applications.

ACKNOWLEDGMENTS

We thank Prof. S.D. Mahanti for insightful discussion. We acknowledge Mr. P. Priyadarshi, Mr. D. Das, and Dr. Tejas Naik for their valuable contribution in preparing this manuscript. This work was supported by CEN Phase-2 and NNETRA projects (Spons/EE/SG-3/2016) at IIT Bombay. The Research and Development work undertaken in the project under the Visvesvaraya Ph.D. Scheme of Ministry of Electronics and Information Technology, Government of India, was implemented by Digital India Corporation (formerly Media Lab Asia). This work was also supported by the Science and Engineering Research Board (SERB) of the Government of India under Grant No. EMR/2017/002853.

APPENDIX A: STRAINED TIGHT-BINDING PARAMETERS

The tight-binding parameters for strain along zigzag direction and armchair direction are given in Tables III and IV, respectively. These parameters are obtained from Ref. [11].

TABLE III. Hopping parameters for zigzag strained graphene.

Strain (%)	$t_1 = t_3$ (in eV)	t_2 (in eV)
0%	2.60	2.60
5%	2.36	2.68
10%	2.08	2.75

TABLE IV. Hopping parameters for armchair strained graphene.

Strain (%)	$t_1 = t_3$ (in eV)	t_2 (in eV)
0%	2.60	2.60
5%	2.55	2.24
10%	2.50	1.88

APPENDIX B: EXPRESSION FOR TRANSMISSION OF GRAPHENE

In Appendix B, we systematically derive the expression for transmission of graphene sheet starting with the expression of mode density of a graphene sub-band using the band counting method.

The mode density of a parabolic sub-band with minima at energy E_1 , is given by

$$M(E) = \Theta(E - E_1). \quad (\text{B1})$$

The function “ $\Theta(E)$ ” denotes a unit step function. Similarly, mode density of three different parabolic sub-bands, each having energy minima at E_1, E_2 , and E_3 is given by

$$M(E) = \sum_{p=1}^3 \Theta(E - E_p). \quad (\text{B2})$$

Similarly, the mode density of a sub-band with energy minima at E_1 and E_2 , and maxima at E_3 (see Fig. 11) is given by

$$M(E) = \sum_{p=1}^2 \Theta(E - E_p) - \Theta(E - E_3). \quad (\text{B3})$$

Likewise, mode density of a sub-band with “ p ” minima and “ q ” maxima is given by

$$M(E) = \sum_{p=1}^p \Theta(E - E_p) - \sum_{q=1}^q \Theta(E - E_q). \quad (\text{B4})$$

In general, Eq. (B4) represents the mode density of a conduction band. The band structure of graphene is symmetric about k_x and k_y axes as well as the energy axis. Thus, a sub-band along armchair or zigzag direction has the same number of modes along forward and backward directions. The conduction and valence bands are symmetric about the energy axis. Thus, the collective equation for mode density of a graphene sub-band (say “ k_{\perp} ”) consisting of the conduction

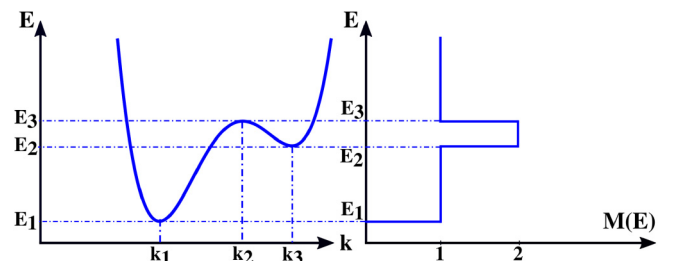


FIG. 11. A sub-band with minima at E_1, E_2 and maxima at E_3 , and its corresponding mode density function.

band and valence band is given by

$$M_{k_{\perp}}^i(E) = \sum_{p=1}^p \Theta(E \mp E_p^i) - \sum_{q=1}^q \Theta(E \mp E_q^i), \quad (\text{B5})$$

where “ i ” is the magnitude of strain in percentage. The negative signs in Eq. (B5) are used for conduction band, whereas the positive signs are used for valence band. We use Eq. (B5) to calculate the mode density function of graphene.

The mode density of TMs inside the segment Δk (see Fig. 4) is given by

$$M_{k_{\perp}}^{i'}(E) = \frac{M_{k_{\perp}}^i(E) * \Delta k}{\delta k}. \quad (\text{B6})$$

$\Delta k = \Delta k_y$ for transport along the armchair direction, and $\Delta k = \Delta k_x$ for transport along the zigzag direction. δk is the separation between adjacent TMs and has a value of $\frac{2\pi}{L_{cs}^i}$.

Therefore, Eq. (B6) simplifies into

$$M_{k_{\perp}}^{i'}(E) = \frac{M_{k_{\perp}}^i(E) * \Delta k * L_{cs}^i}{2\pi}. \quad (\text{B7})$$

Therefore, transmission per unit cross-sectional length due to TMs present inside the segment Δk containing the sub-band (k_{\perp}) is given by

$$T_{k_{\perp}}^i(E) = \frac{M_{k_{\perp}}^i(E) * \Delta k}{2\pi}. \quad (\text{B8})$$

From Eq. (B8), the prefactor ($P_{k_{\perp}}^i$) is given by

$$P_{k_{\perp}}^i = \frac{\Delta k}{2\pi}. \quad (\text{B9})$$

Equivalently, $T_{k_{\perp}}^i(E)$ can be written as

$$\therefore T_{k_{\perp}}^i(E) = P_{k_{\perp}}^i * M_{k_{\perp}}^i(E). \quad (\text{B10})$$

Finally, the total transmission per unit cross-sectional length of graphene sheet at $i\%$ strain when “ j ” segments are used is given by

$$T^i(E) = \sum_{k_{\perp}=1}^j T_{k_{\perp}}^i(E). \quad (\text{B11})$$

APPENDIX C: EXPRESSION FOR GAUGE FACTOR IN BALLISTIC REGIME

The expression for gauge factor is given by

$$GF = \frac{R^i - R^0}{R^0 \varepsilon}, \quad (\text{C1})$$

where R^i is resistance of graphene sheet at $i\%$ strain and R^0 is resistance of graphene sheet at 0% strain. The resistance R^i at $i\%$ strain is given by

$$R^i = \frac{r^i}{L_{cs}^i} = \frac{r^i}{L_{cs} * (1 + \nu \varepsilon)}, \quad (\text{C2})$$

where r^i is the gradient of voltage and current density in the linear regime at $i\%$ strain. From Eqs. (C1) and (C2), the final expression of GF is obtained which is given by

$$GF = \frac{1}{\varepsilon} \left[\frac{r^i}{r^0(1 + \nu \varepsilon)} - 1 \right]. \quad (\text{C3})$$

APPENDIX D: EXPRESSION FOR GAUGE FACTOR IN DIFFUSIVE REGIME

The expression for GF in diffusive regime is obtained from Eq. (14) and $R = \rho \frac{L}{L_{cs}}$. Due to the difference in the direction of electron transport and applied strain in S_1 and S_2 configurations, the expressions for LGF and TGF are different.

From Eq. (14), we obtain

$$\frac{\Delta \rho}{\rho} = \frac{-2\Delta v_f}{v_f}. \quad (\text{D1})$$

From $R = \rho \frac{L}{L_{cs}}$, we obtain

$$\frac{\Delta R}{R} = \frac{\Delta \rho}{\rho} + \frac{\Delta L}{L} - \frac{\Delta L_{cs}}{L_{cs}}. \quad (\text{D2})$$

The simplified expression for LGF using Eqs. (D2), (D1), $\varepsilon = \frac{\Delta L}{L}$, and $\frac{\Delta L_{cs}}{L_{cs}} = \nu \varepsilon$ is given by

$$\text{LGF} = 1 + |\nu| - 2 \frac{\Delta v_f / v_f}{\varepsilon}. \quad (\text{D3})$$

Similarly, the simplified expression for TGF using Eqs. (D2), (D1), $\varepsilon = \frac{\Delta L_{cs}}{L_{cs}}$, and $\frac{\Delta L}{L} = \nu \varepsilon$ is given by

$$\text{TGF} = -(1 + |\nu|) - 2 \frac{\Delta v_f / v_f}{\varepsilon} \quad (\text{D4})$$

-
- [1] A. K. Geim, *Science* **324**, 1530 (2009).
 [2] K. S. Novoselov, V. Fal, L. Colombo, P. Gellert, M. Schwab, and K. Kim, *Nature (London)* **490**, 192 (2012).
 [3] C. Lee, X. Wei, J. W. Kysar, and J. Hone, *Science* **321**, 385 (2008).
 [4] F. Liu, P. Ming, and J. Li, *Phys. Rev. B* **76**, 064120 (2007).
 [5] K. S. Kim, Y. Zhao, H. Jang, S. Y. Lee, J. M. Kim, K. S. Kim, J.-H. Ahn, P. Kim, J.-Y. Choi, and B. H. Hong, *Nature (London)* **457**, 706 (2009).
 [6] F. Guinea, M. I. Katsnelson, and M. A. H. Vozmediano, *Phys. Rev. B* **77**, 075422 (2008).
 [7] F. Guinea, M. Katsnelson, and A. Geim, *Nat. Phys.* **6**, 30 (2010).
 [8] N. Levy, S. Burke, K. Meaker, M. Panlasigui, A. Zettl, F. Guinea, A. C. Neto, and M. Crommie, *Science* **329**, 544 (2010).
 [9] M. Farjam and H. Rafii-Tabar, *Phys. Rev. B* **80**, 167401 (2009).
 [10] Z. H. Ni, T. Yu, Y. H. Lu, Y. Y. Wang, Y. P. Feng, and Z. X. Shen, *ACS Nano* **3**, 483 (2009).
 [11] R. M. Ribeiro, V. M. Pereira, N. M. R. Peres, P. R. Briddon, and A. H. C. Neto, *New J. Phys.* **11**, 115002 (2009).
 [12] S.-M. Choi, S.-H. Jhi, and Y.-W. Son, *Phys. Rev. B* **81**, 081407(R) (2010).

- [13] M. Huang, H. Yan, T. F. Heinz, and J. Hone, *Nano Lett.* **10**, 4074 (2010).
- [14] C. Si, Z. Liu, W. Duan, and F. Liu, *Phys. Rev. Lett.* **111**, 196802 (2013).
- [15] Z. F. Wang, Y. Zhang, and F. Liu, *Phys. Rev. B* **83**, 041403(R) (2011).
- [16] M. F. El-Kady, V. Strong, S. Dubin, and R. B. Kaner, *Science* **335**, 1326 (2012).
- [17] T. Georgiou, R. Jalil, B. D. Belle, L. Britnell, R. V. Gorbachev, S. V. Morozov, Y.-J. Kim, A. Gholinia, S. J. Haigh, O. Makarovskiy, L. Eaves, L. A. Ponomarenko, A. K. Geim, K. S. Novoselov, and A. Mishchenko, *Nat. Nanotech.* **8**, 100 (2012).
- [18] T. Das, B. K. Sharma, A. K. Katiyar, and J.-H. Ahn, *J. Semicond.* **39**, 011007 (2018).
- [19] A. D. Smith, F. Niklaus, A. Paussa, S. Vaziri, A. C. Fischer, M. Sterner, F. Forsberg, A. Delin, D. Esseni, P. Palestri, M. Östling, and M. C. Lemme, *Nano Lett.* **13**, 3237 (2013).
- [20] M. Huang, T. A. Pascal, H. Kim, W. A. Goddard, and J. R. Greer, *Nano Lett.* **11**, 1241 (2011).
- [21] A. D. Smith, F. Niklaus, A. Paussa, S. Schröder, A. C. Fischer, M. Sterner, S. Wagner, S. Vaziri, F. Forsberg, D. Esseni, M. Östling, and M. C. Lemme, *ACS Nano* **10**, 9879 (2016).
- [22] S.-E. Zhu, M. Krishna Ghatkesar, C. Zhang, and G. C. A. M. Janssen, *Appl. Phys. Lett.* **102**, 161904 (2013).
- [23] Y. Lee, S. Bae, H. Jang, S. Jang, S.-E. Zhu, S. H. Sim, Y. I. Song, B. H. Hong, and J.-H. Ahn, *Nano Lett.* **10**, 490 (2010).
- [24] H. Hosseinzadegan, C. Todd, A. Lal, M. Pandey, M. Levendorf, and J. Park, in *Proceedings of the IEEE 25th International Conference on Micro Electro Mechanical Systems (MEMS)* (IEEE, Piscataway, NJ, 2012), pp. 611–614.
- [25] X. Chen, X. Zheng, J.-K. Kim, X. Li, and D.-W. Lee, *J. Vac. Sci. Technol. B* **29**, 06FE01 (2011).
- [26] M. Y. Han, B. Özyilmaz, Y. Zhang, and P. Kim, *Phys. Rev. Lett.* **98**, 206805 (2007).
- [27] S. Adam and S. D. Sarma, *Solid State Commun.* **146**, 356 (2008).
- [28] K. S. Novoselov, A. K. Geim, S. V. Morozov, D. Jiang, Y. Zhang, S. V. Dubonos, I. V. Grigorieva, and A. A. Firsov, *Science* **306**, 666 (2004).
- [29] A. H. Castro Neto, F. Guinea, N. M. R. Peres, K. S. Novoselov, and A. K. Geim, *Rev. Mod. Phys.* **81**, 109 (2009).
- [30] C. Jeong, R. Kim, M. Luisier, S. Datta, and M. Lundstrom, *J. Appl. Phys.* **107**, 023707 (2010).
- [31] V. M. Pereira, A. H. Castro Neto, and N. M. R. Peres, *Phys. Rev. B* **80**, 045401 (2009).
- [32] S. Datta, *Lessons from Nanoelectronics*, 2nd ed. (World Scientific, Singapore, 2017).
- [33] N. M. R. Peres, J. M. B. Lopes dos Santos, and T. Stauber, *Phys. Rev. B* **76**, 073412 (2007).
- [34] K. S. Novoselov, A. K. Geim, S. Morozov, D. Jiang, M. I. Katsnelson, I. Grigorieva, S. Dubonos, and A. A. Firsov, *Nature (London)* **438**, 197 (2005).
- [35] X. Xiao, L. Yuan, J. Zhong, T. Ding, Y. Liu, Z. Cai, Y. Rong, H. Han, J. Zhou, and Z. L. Wang, *Adv. Mater.* **23**, 5440 (2011).
- [36] C. S. Boland, U. Khan, C. Backes, A. O'Neill, J. McCauley, S. Duane, R. Shanker, Y. Liu, I. Jurewicz, A. B. Dalton, and J. N. Coleman, *ACS Nano* **8**, 8819 (2014).